APPLIED PHYSICS

Dendritic patterns from shear-enhanced anisotropy in nematic liquid crystals

Qing Zhang[1]*, Shuang Zhou[2]*, Rui Zhang[3], Irmgard Bischofberger[1]*

Controlling the growth morphology of fluid instabilities is challenging because of their self-amplified and non-linear growth. The viscous fingering instability, which arises when a less viscous fluid displaces a more viscous one, transitions from exhibiting dense-branching growth characterized by repeated tip splitting of the growing fingers to dendritic growth characterized by stable tips in the presence of anisotropy. We controllably induce such a morphology transition by shear-enhancing the anisotropy of nematic liquid crystal solutions. For fast enough flow induced by the finger growth, the intrinsic tumbling behavior of lyotropic chromonic liquid crystals can be suppressed, which results in a flow alignment of the material. This microscopic change in the director field occurs as the viscous torque from the shear flow becomes dominant over the elastic torque from the nematic potential and macroscopically enhances the liquid crystal anisotropy to induce the transition to dendritic growth.

INTRODUCTION

Spontaneous pattern growth at an unstable interface between two fluids is a common phenomenon in many nonequilibrium systems (1–6). A famous example is the viscous fingering instability, in which one fluid is displaced by another less viscous one in the quasi two-dimensional geometry of a Hele-Shaw cell (7). In this instability, fingers of the displacing fluid grow into the displaced one and undergo successive tip splitting, which leads to ramified patterns with many branches that belong to the class of dense-branching growth (8–10). The ubiquitous tip splitting can be prevented by introducing anisotropy in the interfacial dynamics, which stabilizes the fingertips into parabolic shapes; the resulting pattern transitions to dendritic growth (1, 11–16). Dense-branching growth and dendritic growth are two essential morphologies that emerge in a diverse range of physical phenomena, including electrochemical deposition and the growth of bacteria colonies (3, 4, 17–19).

Given the important role of anisotropy in selecting the growth morphology, various experimental methods have been developed to introduce anisotropy in the viscous fingering instability (20–25). The most well-established means is to geometrically modify the growth environment by engraving ordered channels on one of the plates of the Hele-Shaw cell (16, 26, 27). Another strategy is to use a non-Newtonian fluid as one of the fluids, where the anisotropy is an intrinsic property of the medium itself. Theoretical work and numerical simulations have suggested that the local decrease in viscosity in front of the fingertip occurring in shear-thinning visco-elastic fluids can suppress tip splitting by introducing a preferred growth direction (28–31). Experimentally, intrinsically anisotropic thermotropic liquid crystals (TLCs) have been used as the displaced fluid (32). Most TLCs in the nematic phase are flow-aligned materials (33), for which the director maintains a stable angle in the shear plane set by the viscous torques acting on the director (34).

The flow alignment gives rise to a smaller viscosity parallel to the flow direction compared to that perpendicular to the flow direction (34). This difference in viscosities leads to a direction-dependent velocity of the interface and introduces anisotropy in the interfacial dynamics, causing the transition from dense-branching to dendritic growth (34). The flow alignment occurs when the viscous torque from the shear flow becomes dominant over the Frank elastic torque produced by the gradient in the continuum director field; this condition is reached when the Ericksen number is larger than unity (35).

Here, we demonstrate a different pathway to dendritic growth that occurs at much higher Ericksen numbers deep in the flow-dominated regime. We observe this pathway when low-viscosity silicone oil displaces a solution of nematic lyotropic chromonic liquid crystals (LCLCs). LCLCs are aqueous dispersions of organic disk-like molecules that self-assemble into cylindrical aggregates, which are responsible for the formation of liquid crystal phases (36–41). In contrast to most nematic TLCs that flow-align for Ericksen numbers Er > 1, nematic LCLCs exhibit a flow-tumbling behavior where the material does not adopt a stable director field but experiences a nonzero viscous torque acting on the director. In this tumbling state, defects can form in the nematic LCLC solutions (33, 42). Because LCLC aggregates are about 100 times longer than TLC molecules, their rotational relaxation is slow compared to the time scales of the flow, allowing us to access the regime of Deborah numbers close to unity that is not accessible in TLCs (33, 40). We demonstrate how these unique characteristics lead to dendritic growth in the viscous fingering instability by a mechanism different from that reported for nematic TLCs and over a large range of injection flow rates for different viscosities of the displacing fluid.

We reveal that the morphology transition from dense-branching to dendritic growth necessitates an enhancement of anisotropy of the tumbling nematic liquid crystal solution. In the tumbling state, the viscous fingering instability adopts dense-branching growth. We find that the tumbling behavior can be suppressed by high enough shear leading to a flow alignment of the material, which enhances the LCLC anisotropy and induces the transition to dendritic growth. The shear-enhanced anisotropy is reached

[1]Department of Mechanical Engineering, Massachusetts Institute of Technology, Cambridge, MA 02139, USA. [2]Department of Physics, University of Massachusetts Amherst, Amherst, MA 01003, USA. [3]Department of Physics, Hong Kong University of Science and Technology, Hong Kong, China.
*Corresponding author. Email: zqing@mit.edu (Q.Z.); zhou@physics.umass.edu (S.Z.); irmgard@mit.edu (I.B.)

when the viscous torque induced by the shear flow becomes dominant over the elastic torque from the nematic potential. This provides a quantitative criterion for the growth morphology transition and establishes the relation between the orientation of the LCLC aggregates at the microscale and the growth morphology selection at the macroscale.

In a small region very close to the fingertip of the invading fluid, the LCLC aggregates experience a uniaxial extensional flow induced by the finger growth. We show how LCLC aggregates can break when the uniaxial extensional flow dominates over simple shear flow and how this can locally induce a phase transition of the LCLC solution from the nematic phase to the isotropic phase. Such flow-induced phase transition, which is tunable and reversible, could be exploited in applications using LCLC solutions as flow field sensors.

RESULTS

Growth morphology transition in nematic LCLC solutions

Two distinct pattern morphologies emerge as a nematic solution of the lyotropic chromonic liquid crystal disodium cromoglycate (DSCG) is displaced by a lower-viscosity silicone oil in a radial Hele-Shaw cell. At low volumetric flow rates, fingers grow by repeated tip splitting, which results in the generic dense-branching growth. Above a certain volumetric flow rate, however, the fingertips are stabilized, and the morphology transitions to dendritic growth, as shown in Fig. 1 (A and B). Such a morphology transition occurs for different viscosities of the displacing silicone oils ($\eta_{in} = 0.83$ mPa·s in Fig. 1A and $\eta_{in} = 48$ mPa·s in Fig. 1B). The global features of the patterns depend on the viscosity ratio between the inner displacing and the outer displaced fluid, η_{in}/η_{out}. In particular,

an inner circular region within which the outer fluid is fully displaced appears for larger viscosity ratios (16, 43, 44). To quantify the global features of the patterns, we consider the ratio of the finger length R_f to the radius of the inner circular region R_i, measured when the pattern has grown to an outer radius $R_o = 30$ mm, as shown in the inset of Fig. 1C. The ratio R_f/R_i monotonically decreases with increasing viscosity ratio for both dense-branching patterns and dendritic patterns, similar to the behavior observed for two Newtonian fluids (Fig. 1C and fig. S1). Both the dense-branching and the dendritic patterns are characterized by a well-defined fractal dimension that increases with η_{in}/η_{out}, as shown in fig. S2.

To classify the pattern morphologies into either dense-branching or dendritic growth, we consider the temporal evolution of the fingertip width, w, measured 300 μm behind the fingertip. For dense-branching growth, w increases until it reaches a width of twice the most unstable wavelength set by the competition between surface tension forces and viscous forces (7), whereupon the tip splits and w decreases. By contrast, w remains constant for the stabilized parabolic tips of dendritic patterns, as shown in Fig. 1 (D and E).

Growth morphology transition induced by shear-enhanced anisotropy

To understand what governs the morphology transition from dense-branching to dendritic growth, we measure the optical retardance of the DSCG solutions that gives information about the director field. Imaged under crossed polarizers, the interference color is distinct for the two growth morphologies, as shown in Fig. 2A, indicating differences in the alignment of the director field. We determine the in-plane azimuthal angle, ϕ (Fig. 2B), by adding a static 560-nm full-wave plate optical compensator with
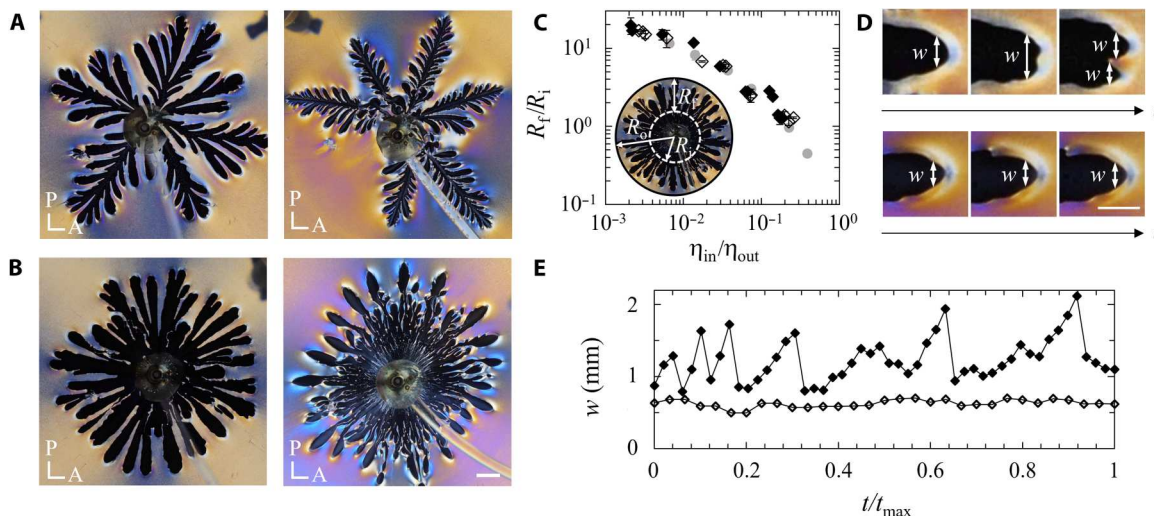

Fig. 1. Morphology transition from dense-branching to dendritic growth observed as silicone oil displaces aqueous solutions of DSCG in the nematic phase. (A and B) With increasing volumetric flow rate q, the pattern transitions from dense-branching growth (left) to dendritic growth (right). (A) Silicone oil viscosity $\eta_{in} = 0.83$ mPa·s and $q = 0.1$ ml/min (left) and $q = 0.4$ ml/min (right). (B) Silicone oil viscosity $\eta_{in} = 48$ mPa·s and $q = 0.05$ ml/min (left) and $q = 1$ ml/min (right). Scale bar, 5 mm. The images are captured using a crossed polarizer, P, and analyzer, A. **(C)** The ratio R_f/R_i when the radius of the pattern reaches $R_o = 30$ mm. The global features of both dense-branching (◆) and dendritic (◇) patterns emerging as silicone oil displaces nematic DSCG solutions are governed by the viscosity ratio, η_{in}/η_{out}, similar to those of dense-branching patterns observed when silicone oil displaces a Newtonian glycerol-water mixture (•). Inset: Definition of the characteristic length scales R_f, R_i, and R_o. **(D)** The width of the fingertip w varies with time t for dense-branching growth characterized by repeated tip splitting (top). The width w remains constant for dendritic growth characterized by stable parabolic tips (bottom). Scale bar, 2 mm. **(E)** Temporal evolution of w for dense-branching growth (◆) and dendritic growth (◇) for $\eta_{in} = 0.83$ mPa·s. t_{max} denotes the time when the fingers reach a length of 30 mm.
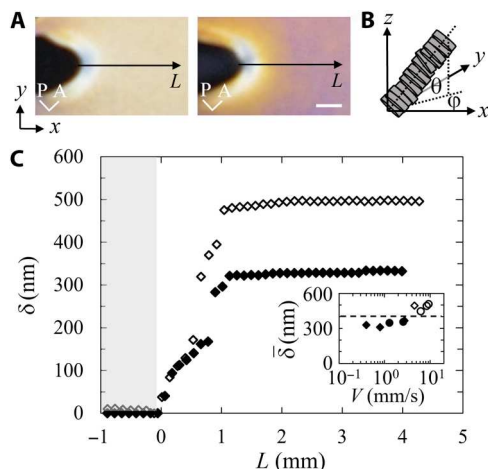
Fig. 2. Distinct director fields for dense-branching and dendritic growth. (A) The difference in color observed in DSCG solutions far from the fingertip denotes distinct director fields for dense-branching growth at $q = 0.05$ ml/min (left) and for dendritic growth at $q = 1$ ml/min (right). We define a local coordinate system where the x axis is in the direction of the fingertip growth, the y axis is perpendicular to the growth direction, and the z axis denotes the direction of the plate spacing. L is the distance from the fingertip along the x direction. Scale bar, 1 mm. **(B)** Schematic of the director orientation. The in-plane azimuthal angle is denoted as ϕ and the out-of-plane polar angle as θ. **(C)** The optical retardance δ along the distance L for dense-branching growth ($\blacklozenge$) and dendritic growth ($\lozenge$). The data correspond to the images in (A). The gray area at $L < 0$ denotes the isotropic oil phase, where the retardance is zero. Inset: Mean optical retardance far from the fingertip averaged over 1.5 mm $< L <$ 4 mm, $\overline{\delta}$, versus the fingertip velocity, V, for silicone oils with viscosities $\eta_{in} = 9.8$ mPa·s ($\bigcirc$) and $\eta_{in} = 48$ mPa·s ($\diamondsuit$). The dashed line marks the transition between dense-branching and dendritic growth.

its slow axis oriented at 45° to the crossed polarizers and find that $\phi \approx 0$; the directors are, on average, uniformly aligned in the radial flow direction for both dense-branching and dendritic growth (see Supplementary Text). The optical retardance, $\delta = \int_0^b | n_{eff}(\theta) - n_o | \, dz = b | n_{eff}(\overline{\theta}) - n_o |$, then provides information about the average out-of-plane polar angle, $\overline{\theta}$, where b is the plate spacing of the Hele-Shaw cell and n_{eff} and n_o are the effective and ordinary refractive indices (45).

Comparing the interference color with a customized Michel-Lévy color chart, we determine the optical retardance δ along the center line in front of a fingertip, L (see Supplementary Text and figs. S3 and S4). In the isotropic oil phase, the retardance is close to zero. Within a small region in front of the fingertip, δ is similar for both types of patterns, as shown in Fig. 2C. Away from the fingertip, however, the retardance is higher for the dendritic pattern than for the dense-branching pattern. These features are consistently observed for different silicone oil viscosities and different fingertip velocities, V, where V is measured at the fingertips as they grow from a radius of $R = 15$ mm to $R = 30$ mm: Dendritic growth occurs beyond a critical value of retardance, as shown in the inset of Fig. 2C.

A low value of retardance in flowing DSCG solutions reflects the tumbling character of the material that leads to a nonzero viscous torque for any orientation of the director with $\alpha_2\alpha_3 < 0$, where α_2 and α_3 are the Leslie viscosity coefficients (35). As a result of the nonzero viscous torque, twist-type topological defects spontaneously occur in the material, which leads to a low retardance (33, 42, 46).

That the viscous fingering instability adopts dense-branching growth in this regime indicates that the tumbling state at the microscale makes the liquid behave isotropically at the macroscale, even for a material that exhibits global nematic ordering. A high value of retardance, by contrast, reflects a small average polar angle ($\overline{\theta} \lesssim 15°$) indicative of a stable flow-aligned state. High shear can thus suppress the tumbling of DSCG solutions. Our results suggest that this transition from tumbling to the flow-aligned state introduces a large enough shear-enhanced anisotropy that allows for the growth morphology transition from dense-branching growth to dendritic growth.

To test this hypothesis, we consider that the morphology transition in DSCG solutions occurs in the regime of high Ericksen number $Er = \frac{\eta_2 \overline{\dot{\gamma}}_{xz} b^2}{K_2}$ ranging from 1.7×10^6 to 9.4×10^7 in our experiments, where η_2 is the twist viscosity, K_2 is the twist Frank elastic constant, and $\overline{\dot{\gamma}}_{xz} = V/b$ is the average shear rate in the xz plane (35, 47). In this regime, the material response is flow dominated. Moreover, given the large size of DSCG aggregates (47), the Deborah number $De = \tau_r/\tau_f \approx 1$, where $\tau_r = 1/D_r$ is the rotational relaxation time of the aggregates, $D_r = \frac{3k_BT[\ln(l/d)-0.8]}{\pi\eta_s l^3}$ is the rotational diffusion coefficient, l is the length and d is the diameter of the DSCG aggregate, η_s is the solvent viscosity, k_B is the Boltzmann constant, T is the temperature, and $\tau_f = 1/\overline{\dot{\gamma}}_{xz}$ is the characteristic time of the shear flow (48). For Deborah numbers of order unity, the director field cannot be considered as a continuum field and the classical Ericksen-Leslie theory does not apply (48). Instead, we need to consider the dynamics of individual molecular aggregates, which is set by the competition between the elastic torque from the nematic potential that induces collective tumbling of the directors and the viscous torque from shear flow that drives individual aggregates to reorient toward the stationary angle adopted in the flow-aligned state. We express the elastic torque acting on the aggregates as $M_{el} = l\frac{dU_{nem}}{dz} \approx l\frac{U_{nem}}{b}$, where U_{nem} is the nematic potential that we express using the Onsager excluded-volume potential $U_{nem} = 2dl^2Ck_BT$, $C = 4\phi/\pi d^2 l$ is the number of aggregates per unit volume, and ϕ is the volume fraction of DSCG in water (40, 49). The viscous torque from the shear flow is $M_{visc} \approx \eta_{eff}\dot{\gamma}_{xz}(z)bl^2$, where $\eta_{eff} \approx \frac{\phi}{dl^2}\xi$ is the effective viscosity that is related to the drag coefficient $\xi \approx \frac{\pi}{6}\eta_s l^3$ (49). The competition between M_{visc} and M_{el} can be expressed by $\Pi = \frac{M_{visc}}{M_{el}} \approx \frac{\pi^2}{48}\frac{\eta_s lb^2\dot{\gamma}_{xz}(z)}{k_BT}$. A similar expression can be more rigorously obtained from the Smoluchowski equation (see Supplementary Text). We consider almost all directors to be flow-aligned when the shear rate in the center region of the gap reaches $\dot{\gamma}_{xz,c} = \frac{12z_c}{b}\overline{\dot{\gamma}}_{xz,c}$, where $\overline{\dot{\gamma}}_{xz,c} = \frac{V^*}{b}$ is the average critical shear rate, V^* is the gap-averaged critical velocity denoting the transition from tumbling to flow alignment, and $z_c \approx 10^{-4}\frac{b}{2}$ is a characteristic length scale denoting the center region chosen of the order of the radius of a DSCG aggregate ($\approx$1 nm). Setting $\Pi = 1$ then yields $V^* \approx \frac{8\times10^4}{\pi^2}\frac{k_BT}{\eta_s lb}$.

We can now probe whether V^* governs the transition from dense-branching to dendritic growth by varying the plate spacing, b, and the length of the aggregates, l. The length of the aggregates can be tuned by using different concentrations of DSCG in water (40, 47). For a set of experiments at a given b and l, the growth morphology transition occurs at a critical fingertip velocity V_c that is

independent of the viscosity of the displacing silicone oil, η_{in}, as shown in Fig. 3 (A and B). Both changing b and l systematically shifts V_c. We can rescale all data by normalizing the fingertip velocity V with V^*, as shown in Fig. 3C. This corroborates that the microscopic transition from tumbling to flow alignment occurring at V^* governs the macroscopic growth morphology transition.

For both nematic TLCs and nematic LCLCs, the transition from dense-branching to dendritic growth occurs as the directors adopt a flow-aligned state. The mechanism that governs the flow alignment, however, is distinct for the two classes of liquid crystals. The flow alignment in nematic TLCs is described within the framework of the Ericksen-Leslie theory, where the dynamics of the director is set by the competition between the Frank elastic torque produced by the gradient of the continuum director field and the viscous torque from the shear flow expressed by the Ericksen number (35). Flow alignment occurs for Er >1. In a tumbling liquid crystal, such as the nematic DSCG solution, by contrast, the flow alignment occurs at much higher Er > 10^6 and at high Deborah numbers De $\approx 10^{-2} - 10^1$ compared to De <10^{-5} for TLCs. In this Deborah number regime, the Ericksen-Leslie theory is not applicable, and instead, molecular theories considering the nematic potential resisting the shear flow deforming individual aggregates, as expressed by Π, describe the flow alignment. Our experiments show that dendritic growth can occur for De $\gtrsim 1$ in nematic tumbling LCLCs, and not only in the previously reported regime of De << 1 in nematic flow–aligned TLCs.

Extensional flow locally breaks DSCG aggregates at fingertips

While the morphology selection is determined by the state of alignment of LCLC aggregates far from the fingertip, the invading oil finger modifies the state of the LCLC aggregates close to the oil-liquid crystal interface. In a small region directly in front of the fingertip, we observe a dark region that denotes a substantial decrease in retardance compared to the region away from the tip, as shown in Fig. 4A. Such a low value of retardance could be due to three

possible effects: (i) a homeotropic alignment ($\theta = 90°$) of the director field, (ii) a twist deformation of the director in the gap direction, or (iii) a decrease of the order parameter (33). To test which of these effects is the cause of the lower retardance, we tilt the Hele-Shaw cell by 20°. We find that the dark area remains dark upon tilting the Hele-Shaw cell, as shown in Fig. 4A, which indicates that the lower retardance is due to a decrease of the order parameter as the two other possible effects would induce a change in retardance upon tilting the cell. The decrease in retardance occurs over a similar range L_c for different volumetric flow rates, as shown in Fig. 4B.

To understand why the order parameter is lower in the region in front of the fingertip, we measure the two-dimensional velocity field v(x, y, t) using tracer particles. The relative velocity of the DSCG solution in the frame of the moving fingertip reveals a combination of uniaxial extensional flow and simple shear flow, as shown by the black arrows in Fig. 4C. The color map of the strain rate calculated as $\dot{\gamma} = \sqrt{\dot{\gamma}_e^2 + \dot{\gamma}_s^2}$ shows that the maximum strain rate occurs in the fingertip region, where $\dot{\gamma}_e = \frac{1}{2}\left(\frac{\partial v_x}{\partial x} - \frac{\partial v_y}{\partial y}\right)$ is the extensional component of the strain rate and $\dot{\gamma}_s = \frac{1}{2}\left(\frac{\partial v_x}{\partial y} + \frac{\partial v_y}{\partial x}\right)$ is the shear component of the strain rate. We hypothesize that the order parameter decreases in the region of high strain rate as a result of the strong extensional flow. This might appear counterintuitive, as extensional flows have been reported to increase the order parameter in rigid rods suspended in a fluid by promoting the rods to align (50, 51). However, distinct from rigid rods, the DSCG aggregates can break and consequently form an isotropic phase (52), which would substantially decrease the order parameter.

To test this hypothesis, we estimate the effect of the extensional flow on the DSCG aggregates by considering (i) the energy balance between the scission energy of aggregates, E_{sci}, which describes the energy required to break an aggregate into two, and the energy input from extensional flow, E_{ext}, and (ii) the alignment of DSCG
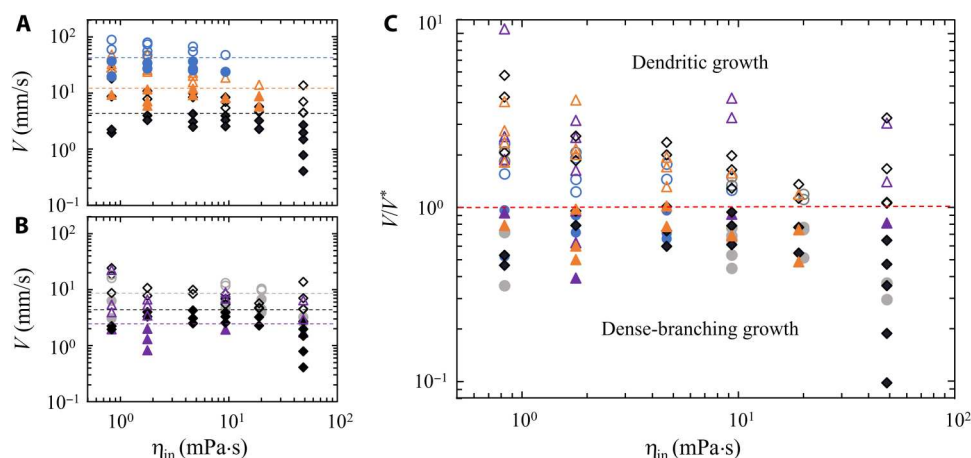

Fig. 3. Morphology diagrams denoting the transition from dense-branching to dendritic growth controlled by the fingertip velocity, *V*. (A) Experiments performed at fixed plate spacing, $b = 25$ μm, for three concentrations of DSCG in water: $c = 14$ wt % (○), $c = 16$ wt % (△), and $c = 18$ wt % (◇). Closed symbols denote dense-branching growth; open symbols denote dendritic growth. The dashed lines mark the transitions between dense-branching growth and dendritic growth occurring at critical fingertip velocities V_c. **(B)** Experiments performed at fixed concentration of DSCG in water, $c = 18$ wt %, for three plate spacings: $b = 12$ μm (○), $b = 25$ μm (◇), and $b = 50$ μm (△). **(C)** Morphology diagram where V is normalized with V^*, the velocity denoting the balance of the elastic torques from the nematic ordering and the viscous torques from the shear flow.
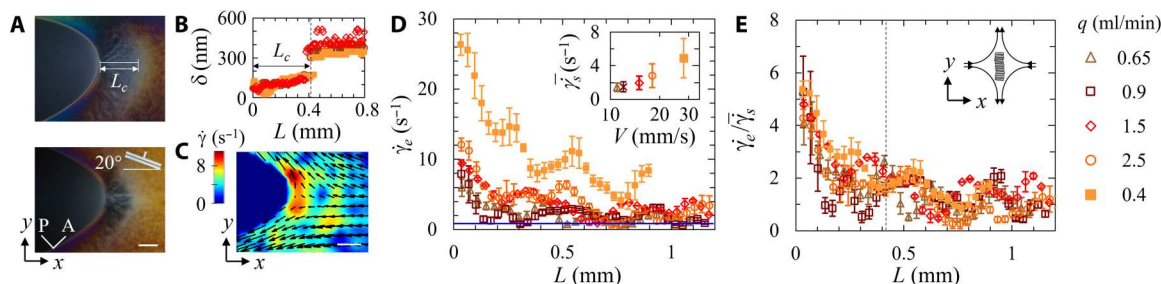
Fig. 4. Extensional shear at the fingertip induces isotropic liquid crystal phase. (**A**) Zoomed image of the fingertip region for a volumetric flow rate $q = 1.5$ ml/min. A dark region of length L_c is seen in front of the fingertip (top), which remains dark upon tilting the Hele-Shaw cell by 20° (bottom). Scale bar, 200 μm. (**B**) Optical retardance, δ, measured at the center line of a finger for experiments at different volumetric flow rates q (see legend to the right). Closed symbols denote $\eta_{in} = 0.83$ mPa·s, open symbols denote $\eta_{in} = 48$ mPa·s. L_c, indicated by the dashed line, denotes the region characterized by a low δ. (**C**) Map of the relative velocity (arrows) in the frame of the moving fingertip and the strain rate $\dot{\gamma}$ (color map) for $q = 1.5$ ml/min. Scale bar, 200 μm. (**D**) Extensional component of the strain rate, $\dot{\gamma}_e$, measured at the center line of a finger versus the distance from the fingertip, L. The blue line denotes the critical extensional component of the strain rate above which an aggregate breaks, $\dot{\gamma}_{e,cr}$. Inset: The mean shear component of the strain rate, $\overline{\dot{\gamma}}_s$, increases with increasing fingertip velocity, V. (**E**) Scaled master curve of $\dot{\gamma}_e / \overline{\dot{\gamma}}_s$ versus L. The dashed line indicates L_c. Inset: A DSCG aggregate aligns parallel to the uniaxial extensional flow when $\dot{\gamma}_e > \overline{\dot{\gamma}}_s$. Strong shear can break the aggregate, which results in the isotropic liquid crystal phase.

aggregates in the extensional flow, which determines whether the aggregates are in tension or in compression.

The scission energy is $E_{sci} \approx 10 k_B T$ (*47*). The energy from extensional flow is expressed as $E_{ext} = \sigma_e \Lambda \phi^{-1}$, where $\sigma_e = -(\alpha_2 + \alpha_3)\dot{\gamma}_e$ is the extensional stress, $\Lambda \approx dl^2$, and ϕ is the volume fraction of DSCG aggregates in water (see Supplementary Text). Balancing the two energies, $E_{sci} = E_{ext}$, yields a critical extensional strain rate inducing breakage of the aggregates, $\dot{\gamma}_{e,cr} \approx 1$ s^{-1}, shown as a blue line in Fig. 4D. The measured extensional component of the strain rate $\dot{\gamma}_e$ intersects $\dot{\gamma}_{e,cr}$ at different distances L from the fingertip for experiments performed at different volumetric flow rates q. This is inconsistent with the independence of L_c on q (Fig. 4B). $\dot{\gamma}_{e,cr}$ denotes the onset of aggregate breakage only for the condition where the aggregates are in tension, which is the case when the aggregates are oriented parallel to the uniaxial extensional direction (inset of Fig. 4E). Conversely, when the aggregates are oriented perpendicular to the uniaxial extensional direction, they are in compression, and $\dot{\gamma}_{e,cr}$ does not induce breakage. To determine the orientation of the aggregates in the fingertip region, we consider that the aggregates undergo a simple shear flow in the x direction that favors alignment in the x direction and an uniaxial extensional flow in the y direction that favors alignment in the y direction (*33, 50, 51*). The competition between $\dot{\gamma}_e$ and $\dot{\gamma}_s$ governs the aggregate orientation. $\dot{\gamma}_s$ is almost constant in the fingertip region (see Supplementary Text and fig. S5), and the mean shear component of the strain rate, $\overline{\dot{\gamma}}_s$, systematically increases with fingertip velocity, as shown in the inset of Fig. 4D. We thus normalize $\dot{\gamma}_e$ with $\overline{\dot{\gamma}}_s$, which rescales all data and shows that $\dot{\gamma}_e / \overline{\dot{\gamma}}_s > 1$ for $L < L_c$, as displayed in Fig. 4E. The DSCG aggregates align in the y direction close to the fingertip and break as $\dot{\gamma}_e > \dot{\gamma}_{e,cr}$, which induces the transition from the nematic to the isotropic phase reflected in the decrease in retardance.

DISCUSSION

We demonstrate how fast flows can suppress the tumbling behavior of nematic LCLC solutions and induce a flow alignment of the director field. As a result of such a shear-enhanced anisotropy of the liquid crystal, the pattern obtained in the viscous fingering instability transitions from dense-branching growth to dendritic growth. We have established a quantitative criterion for this growth morphology transition in terms of the competition between the elastic torque from the nematic potential and the viscous torque from shear flow, which allows us to controllably tune the pattern growth occurring in interfacial fluid instabilities. The resulting interfaces with distinct microscopic alignment and complex shape could be exploited as scaffolds for transmitting anisotropy to surface-active components.

The self-assembled nature of LCLC solutions introduces the potential of aggregate breakage. We show that the high uniaxial extensional shear close to a fingertip during finger growth can break LCLC aggregates and induce a phase transition from the nematic to the isotropic phase. This might be exploited to design flow field sensors with reversible phase transitions that can easily be induced by tuning the flow rate (*53, 54*).

MATERIALS AND METHODS

Our experiments are performed in a radial Hele-Shaw cell consisting of two 19-mm-thick circular glass plates of diameter 140 mm. The spacing between the two plates, b, is maintained by spacers placed around the plate perimeter and varies from 12 to 50 μm. We use silicone oils (Sigma-Aldrich and Consolidated Chemical & Solvents LLC) with viscosities ranging from 0.83 to 48 mPa·s as the displacing inner fluid and aqueous solutions of the LCLC DSCG (purity >98.0%; TCI America) as the displaced outer fluid. We prepare nematic DSCG solutions with concentrations of 14, 16, and 18 weight % (wt%) DSCG in water at room temperature $T = 23 \pm 0.5$°C (*47*). The fluids are injected through a 2-mm-diameter hole in the center of one of the plates at a volumetric flow rate ranging from $q = 0.05$ to 5.5 ml/min controlled by a syringe pump (Harvard PHD 2000). We visualize the patterns through crossed polarizers and record their growth with a LUMIX GH5 camera at frame rates up to 60 fps.

To investigate the director field and the flow field in the region close to the fingertips, we use a smaller Hele-Shaw cell with plate spacing 25 μm, consisting of two 6-mm-thick square glass plates of size 75 mm by 75 mm. The director field is observed through

crossed polarizers in an optical microscope (OMAX M837T) with an objective of magnification $M = 4\times$ and numerical aperture NA = 0.1. The flow field is quantified by tracking polystyrene microspheres (Alpha Nanotech Inc.) of diameter 2 μm using the optical microscope. The microspheres are dispersed in the DSCG solutions at a concentration of 0.05 wt%. The director field and the flow field are captured using a high-speed camera (Chronos 1.4) at frame rates of 1069 fps. We determine the two-dimensional velocity field using a digital particle image velocimetry tool for MATLAB (PIVlab) (55, 56).

Supplementary Materials

This PDF file includes:
Supplementary Text
Figs. S1 to S5
References

Other Supplementary Material for this manuscript includes the following:
Movies S1 and S2

REFERENCES AND NOTES

1. E. Ben-Jacob, P. Garik, The formation of patterns in non-equilibrium growth. *Nature* **343**, 523–530 (1990).
2. F. Gallaire, P.-T. Brun, Fluid dynamic instabilities: Theory and application to pattern forming in complex media. *Phil. Trans. Math. Phys. Eng. Sci.* **375**, 20160155 (2017).
3. X. Cheng, L. Xu, A. Patterson, H. M. Jaeger, S. R. Nagel, Towards the zero-surface-tension limit in granular fingering instability. *Nat. Phys.* **4**, 234–237 (2008).
4. R. Zenit, Some fluid mechanical aspects of artistic painting. *Phys. Rev. Fluids* **4**, 110507 (2019).
5. S. Wei, Z. Cheng, P. Nath, M. D. Tikekar, G. Li, L. A. Archer, Stabilizing electrochemical interfaces in viscoelastic liquid electrolytes. *Sci. Adv.* **4**, eaao6243 (2018).
6. S. Alqatari, T. E. Videbæk, S. R. Nagel, A. E. Hosoi, I. Bischofberger, Confinement-induced stabilization of the Rayleigh-Taylor instability and transition to the unconfined limit. *Sci. Adv.* **6**, eabd6605 (2020).
7. P. G. Saffman, G. I. Taylor, The penetration of a fluid into a porous medium or Hele-Shaw cell containing a more viscous liquid. *Proc. R. Soc. Lond. A* **245**, 312–329 (1958).
8. E. Ben-Jacob, G. Deutscher, P. Garik, N. D. Goldenfeld, Y. Lareah, Formation of a dense branching morphology in interfacial growth. *Phys. Rev. Lett.* **57**, 1903–1906, 1906 (1986).
9. L. Paterson, Radial fingering in a Hele Shaw cell. *J. Fluid Mech.* **113**, 513–529 (1981).
10. F. M. Orr Jr., J. J. Taber, Use of carbon dioxide in enhanced oil recovery. *Science* **224**, 563–569 (1984).
11. J. S. Langer, Instabilities and pattern formation in crystal growth. *Rev. Mod. Phys.* **52**, 28 (1980).
12. J. S. Langer, Dendrites, viscous fingers, and the theory of pattern formation. *Science* **243**, 1150–1156 (1989).
13. Y. Couder, F. Argoul, A. Arnéodo, J. Maurer, M. Rabaud, Statistical properties of fractal dendrites and anisotropic diffusion-limited aggregates. *Phys. Rev. A* **42**, 3499–3503 (1990).
14. E. Ben-Jacob, N. Goldenfeld, J. S. Langer, G. Schön, Dynamics of interfacial pattern formation. *Phys. Rev. Lett.* **51**, 1930–1932 (1983).
15. H. Yasuda, K. Morishita, N. Nakatsuka, T. Nishimura, M. Yoshiya, A. Sugiyama, K. Uesugi, A. Takeuchi, Dendrite fragmentation induced by massive-like $\delta - \gamma$ transformation in Fe–C alloys. *Nat. Commun.* **10**, 3183 (2019).
16. Q. Zhang, A. Amooie, M. Z. Bazant, I. Bischofberger, Growth morphology and symmetry selection of interfacial instabilities in anisotropic environments. *Soft Matter* **17**, 1202–1209 (2021).
17. S. Parsa, E. Santanach-Carreras, L. Xiao, D. A. Weitz, Origin of anomalous polymer-induced fluid displacement in porous media. *Phys. Rev. Fluids* **5**, 022001 (2020).
18. M. E. Rosti, S. Pramanik, L. Brandt, D. Mitra, The breakdown of Darcy's law in a soft porous material. *Soft Matter* **16**, 939–944 (2020).
19. Z. Ahmad, Z. Hong, V. Viswanathan, Design rules for liquid crystalline electrolytes for enabling dendrite-free lithium metal batteries. *Proc. Natl. Acad. Sci. U.S.A.* **117**, 26672–26680 (2020).
20. K. V. McCloud, J. V. Maher, Experimental perturbations to Saffman-Taylor flow. *Phys. Rep.* **260**, 139–185 (1995).
21. Y. Couder, O. Cardoso, D. Dupuy, P. Tavernier, W. Thom, Dendritic growth in the Saffman-Taylor experiment. *EPL* **2**, 437–443 (1986).
22. G. Zocchi, B. E. Shaw, A. Libchaber, L. P. Kadanoff, Finger narrowing under local perturbations in the Saffman-Taylor problem. *Phys. Rev. A* **36**, 1894–1900 (1987).
23. T. Tóth-Katona, A. Buka, Nematic-liquid-crystal–air interface in a radial Hele-Shaw cell: Electric field effects. *Phys. Rev. E* **67**, 041717 (2003).
24. L. Ducloué, A. L. Hazel, D. Pihler-Puzović, A. Juel, Viscous fingering and dendritic growth under an elastic membrane. *J. Fluid Mech.* **826**, R2 (2017).
25. A. Juel, D. Pihler-Puzović, M. Heil, Instabilities in blistering. *Annu. Rev. Fluid Mech.* **50**, 691–714 (2018).
26. E. Ben-Jacob, R. Godbey, N. D. Goldenfeld, J. Koplik, H. Levine, T. Mueller, L. Sander, Experimental demonstration of the role of anisotropy in interfacial pattern formation. *Phys. Rev. Lett.* **55**, 1315–1318 (1985).
27. J.-D. Chen, Radial viscous fingering patterns in Hele-Shaw cells. *Exp. Fluids* **5**, 363–371 (1987).
28. L. Kondic, M. J. Shelley, P. Palffy-Muhoray, Non-Newtonian Hele-Shaw flow and the Saffman-Taylor instability. *Phys. Rev. Lett.* **80**, 1433–1436 (1998).
29. P. Fast, L. Kondic, M. J. Shelley, P. Palffy-Muhoray, Pattern formation in non-Newtonian Hele-Shaw flow. *Phys. Fluids* **13**, 1191–1212 (2001).
30. J. V. Fontana, H. Gadêlha, J. A. Miranda, Development of tip-splitting and side-branching patterns in elastic fingering. *Phys. Rev. E* **93**, 033126 (2016).
31. Y. Lee, J. Azaiez, I. Gates, Interfacial instabilities of immiscible non-Newtonian radial displacements in porous media. *Phys. Fluids* **31**, 043103 (2019).
32. A. Buka, J. Kertész, T. Vicsek, Transitions of viscous fingering patterns in nematic liquid crystals. *Nature* **323**, 424–425 (1986).
33. H. Baza, T. Turiv, B.-X. Li, R. Li, B. M. Yavitt, M. Fukuto, O. D. Lavrentovich, Shear-induced polydomain structures of nematic lyotropic chromonic liquid crystal disodium cromoglycate. *Soft Matter* **16**, 8565–8576 (2020).
34. A. Buka, P. Palffy-Muhoray, Z. Racz, Viscous fingering in liquid crystals. *Phys. Rev. A* **36**, 3984–3989 (1987).
35. M. Kleman, O. D. Lavrentovich, *Soft matter physics: An introduction* (Springer Science & Business Media, 2007).
36. H.-S. Park, S.-W. Kang, L. Tortora, Y. Nastishin, D. Finotello, S. Kumar, O. D. Lavrentovich, Self-assembly of lyotropic chromonic liquid crystal Sunset Yellow and effects of ionic additives. *J. Phys. Chem. B* **112**, 16307–16319 (2008).
37. M. P. Renshaw, I. J. Day, NMR characterization of the aggregation state of the azo dye sunset yellow in the isotropic phase. *J. Phys. Chem. B* **114**, 10032–10038 (2010).
38. J. Lydon, Chromonic liquid crystalline phases. *Liq. Cryst.* **38**, 1663–1681 (2011).
39. S. Zhou, Y. A. Nastishin, M. M. Omelchenko, L. Tortora, V. G. Nazarenko, O. P. Boiko, T. Ostapenko, T. Hu, C. C. Almasan, S. N. Sprunt, J. T. Gleeson, O. D. Lavrentovich, Elasticity of lyotropic chromonic liquid crystals probed by director reorientation in a magnetic field. *Phys. Rev. Lett.* **109**, 037801 (2012).
40. S. Zhou, K. Neupane, Y. A. Nastishin, A. R. Baldwin, S. V. Shiyanovskii, O. D. Lavrentovich, S. Sprunt, Elasticity, viscosity, and orientational fluctuations of a lyotropic chromonic nematic liquid crystal disodium cromoglycate. *Soft Matter* **10**, 6571–6581 (2014).
41. P. J. Collings, J. N. Goldstein, E. J. Hamilton, B. R. Mercado, K. J. Nieser, H. H. Regan, The nature of the assembly process in chromonic liquid crystals. *Liq. Cryst. Rev.* **3**, 1–27 (2015).
42. Q. Zhang, R. Zhang, B. Ge, Z. Yaqoob, P. T. So, I. Bischofberger, Structures and topological defects in pressure-driven lyotropic chromonic liquid crystals. *Proc. Natl. Acad. Sci. U.S.A.* **118**, e2108361118 (2021).
43. I. Bischofberger, R. Ramachandran, S. R. Nagel, Fingering versus stability in the limit of zero interfacial tension. *Nat. Commun.* **5**, 5265 (2014).
44. I. Bischofberger, R. Ramachandran, S. R. Nagel, An island of stability in a sea of fingers: Emergent global features of the viscous-flow instability. *Soft Matter* **11**, 7428–7432 (2015).
45. P. Yeh, C. Gu, *Optics of Liquid Crystal Displays* (John Wiley & Sons, 2009), vol. 67.
46. B. Ge, Q. Zhang, R. Zhang, J.-T. Lin, P.-H. Tseng, C.-W. Chang, C.-Y. Dong, R. Zhou, Z. Yaqoob, I. Bischofberger, P. T. C. So, Single-shot quantitative polarization imaging of complex birefringent structure dynamics. *ACS Photonics* **8**, 3440–3447 (2021).
47. S. Zhou, Elasticity, viscosity, and orientational fluctuations of a lyotropic chromonic nematic liquid crystal disodium cromoglycate, in *Lyotropic Chromonic Liquid Crystals: From Viscoelastic Properties to Living Liquid Crystals* (Springer, 2017), pp. 67–102.
48. R. G. Larson, *The Structure and Rheology of Complex Fluids* (Oxford University Press, 1999).
49. R. Larson, Arrested tumbling in shearing flows of liquid-crystal polymers. *Macromolecules* **23**, 3983–3992 (1990).
50. V. Calabrese, S. J. Haward, A. Q. Shen, Effects of shearing and extensional flows on the alignment of colloidal rods. *Macromolecules* **54**, 4176–4185 (2021).

51. M. Trebbin, D. Steinhauser, J. Perlich, A. Buffet, S. V. Roth, W. Zimmermann, J. Thiele, S. Förster, Anisotropic particles align perpendicular to the flow direction in narrow microchannels. *Proc. Natl. Acad. Sci. U.S.A.* **110**, 6706–6711 (2013).

52. S. Zhou, S. V. Shiyanovskii, H.-S. Park, O. D. Lavrentovich, Fine structure of the topological defect cores studied for disclinations in lyotropic chromonic liquid crystals. *Nat. Commun.* **8**, 14974 (2017).

53. S. V. Shiyanovskii, O. D. Lavrentovich, T. Schneider, T. Ishikawa, I. I. Smalyukh, C. J. Woolverton, G. D. Niehaus, K. J. Doane, Lyotropic chromonic liquid crystals for biological sensing applications. *Mol. Cryst. Liq.* **434**, 259–270 (2007).

54. P. Popov, L. W. Honaker, E. E. Kooijman, E. K. Mann, A. I. Jákli, A liquid crystal biosensor for specific detection of antigens. *Sens. Bio-Sens. Res.* **8**, 31–35 (2016).

55. W. Thielicke, E. Stamhuis, PIVlab–Towards user-friendly, affordable and accurate digital particle image velocimetry in matlab. *J. Open Res. Softw.* **2**, e30 (2014).

56. W. Thielicke, R. Sonntag, Particle image velocimetry for MATLAB: Accuracy and enhanced algorithms in PIVlab. *J. Open Res. Softw.* **9**, 12 (2021).

57. J. Nittmann, G. Daccord, H. E. Stanley, Fractal growth viscous fingers: Quantitative characterization of a fluid instability phenomenon. *Nature* **314**, 141–144 (1985).

58. E. L. Hinrichsen, K. Måløy, J. Feder, T. Jossang, Self-similarity and structure of dla and viscous fingering clusters. *J. Phys. A* **22**, L271 (1999).

59. O. Praud, H. L. Swinney, Fractal dimension and unscreened angles measured for radial viscous fingering. *Phys. Rev. E* **72**, 011406 (2005).

60. J. Mathiesen, I. Procaccia, H. L. Swinney, M. Thrasher, The universality class of diffusion-limited aggregation and viscous fingering. *Europhys. Lett.* **76**, 257, 263 (2006).

61. B. E. Sørensen, A revised Michel-Lévy interference colour chart based on first-principles calculations. *Eur. J. Mineral.* **25**, 5–10 (2013).

62. Y. A. Nastishin, H. Liu, T. Schneider, V. Nazarenko, R. Vasyuta, S. V. Shiyanovskii, O. D. Lavrentovich, Optical characterization of the nematic lyotropic chromonic liquid crystals: Light absorption, birefringence, and scalar order parameter. *Phys. Rev. E* **72**, 041711 (2005).

63. H. Yu, P. Zhang, A kinetic–hydrodynamic simulation of microstructure of liquid crystal polymers in plane shear flow. *J. Non-Newton. Fluid Mech.* **141**, 116–127 (2007).